APL Materials

Anisotropic, meandering domain microstructure in the improper ferroelectric $CsNbW_2O_9$

Cite as: APL Mater. **8**, 101108 (2020); https://doi.org/10.1063/5.0026040
Submitted: 20 August 2020 . Accepted: 05 October 2020 . Published Online: 19 October 2020

Shane J. McCartan, Patrick W. Turner, Jason A. McNulty, Jesi R. Maguire, Conor J. McCluskey, Finlay D. Morrison, J. Marty Gregg, and Ian MacLaren

Anisotropic, meandering domain microstructure in the improper ferroelectric $CsNbW_2O_9$

Cite as: APL Mater. 8, 101108 (2020); doi: 10.1063/5.0026040
Submitted: 20 August 2020 • Accepted: 5 October 2020 •
Published Online: 19 October 2020

Shane J. McCartan,[1,2] Patrick W. Turner,[2] Jason A. McNulty,[3] Jesi R. Maguire,[2] Conor J. McCluskey,[2] Finlay D. Morrison,[3] J. Marty Gregg,[2] and Ian MacLaren[1,a)]

AFFILIATIONS

[1]School of Physics and Astronomy, University of Glasgow, Glasgow G12 8QQ, United Kingdom
[2]School of Mathematics and Physics, Queen's University Belfast, Belfast BT7 1NN, United Kingdom
[3]EaStCHEM School of Chemistry, University of St Andrews, St Andrews KY16 9ST, United Kingdom

Note: This paper is part of the Special Topic on 100 Years of Ferroelectricity—A Celebration.
[a)]**Author to whom correspondence should be addressed:** ian.maclaren@glasgow.ac.uk

ABSTRACT

The improper ferroelectric $CsNbW_2O_9$ has recently been highlighted as the first material outside the manganite family to exhibit a similar meandering, sixfold domain structure to that responsible for enhanced and diminished conduction at charged domain walls in the rare earth manganites. While there is no current evidence for variation in domain wall conduction relative to bulk in $CsNbW_2O_9$, the similarities in microstructure strongly suggest that charged domain walls are present in this material. Herein, we report a comprehensive study of the domain microstructure of $CsNbW_2O_9$ by both piezoresponse force microscopy and transmission electron microscopy to reveal that there are, in fact, clear distinctions in the domain structure of the two systems. Constraints arising from the crystal structure of $CsNbW_2O_9$, namely, the connectivity of the BO_6 polyhedra and atomic displacements occurring purely along the *c* axis, mean that domain walls preferentially run parallel to the *c* direction (the polar axis of the material) and thus remain uncharged. The characteristic cloverleaf domain structure reminiscent of the manganites is still present; however, the structure meanders predominantly in the *ab* plane and, therefore, appears differently depending on the projection direction from which it is viewed. As a result of this microstructural constraint, charged domain walls are not prevalent in this material.

I. INTRODUCTION

In recent years, ferroelectrics research has undergone a dramatic shift in focus, which has led to the development of a new field in its own right. Surprisingly, this shift was not driven by the discovery of new materials but by closer examination of the microstructure in known systems with an emphasis on regions that had previously been disregarded. The interface separating two domains of the uniform order parameter (termed a domain wall) has come to the forefront of research with the discovery of various functionality in different systems, such as superconductivity in the domain walls of WO_{3-x},[1] magnetism in the domain walls of $TbMnO_3$,[2] and ferrielectricity in the ferroelastic domain walls of $CaTiO_3$.[3] Particular interest has been generated by "charged" ferroelectric domain walls in which like bound charges on either side of the wall generate divergence in the electric displacement field; this can be associated with enhanced or diminished electrical conduction relative to the bulk. In fact, the conductivity can vary by up to 14 orders of magnitude between a charged and neutral wall.[4] Since their discovery, charged conducting domain walls have been observed in an abundance of ferroelectric materials, such as $BiFeO_3$,[5] $LiNbO_3$,[6] $BaTiO_3$,[7] $(Ca, Sr)_3Ti_2O_7$,[8] $Cu_3B_7O_{13}Cl$,[9] and $RMnO_3$ (R = Sc, Y, Dy–Lu).[10] With a wealth of discoveries, the field of domain wall nanoelectronics was established—a possible avenue for device miniaturization to continue in accordance with Moore's law, using completely new device paradigms. Such ideas have already come to fruition with the development of domain wall diode and tunnel junction devices.[11–13] To date, the hexagonal rare-earth manganites ($RMnO_3$)

have been one of the most intensively studied systems for domain wall conduction, as the domain microstructure guarantees charged wall sections of both *p*-type and *n*-type alongside neutral walls in the same sample.[10,14,15] They also represent the first materials in which the conduction properties of the domain walls have been characterized with Hall effect measurements.[14,15] The manganites exhibit improper ferroelectricity arising from the coupling of the K_3 nonpolar mode and the Γ_2^- polar mode. The K_3 "trimerization" mode is the primary order parameter that causes tilting of the MnO_5 polyhedra and a "two-up, one-down" displacement of the A site cations along the *c* axis, thus tripling the unit cell. It is the coupling of the polar Γ_2^- mode to the cell-tripling (non-polar) K_3 mode that results in a net cation displacement along *c* and thus why the subsequent ferroelectricity is improper.[16] The resulting domain structure has six energetically equivalent variants—three translational variants due to the cell tripling (denoted as α, β, and γ ambiguously), each exhibiting a polar variant (+ and −). These six domain variants coalesce at cloverleaf vertices, between which the domain walls meander isotropically throughout the material. It is the meandering nature of the microstructure in three dimensions, in combination with the system's uniaxial polarization, that guarantees the formation of charged "head-to-head" and "tail-to-tail" wall sections, which are most often associated with enhanced or diminished conduction.

Until recently, these manganites were the only family of ferroelectrics known to exhibit such a domain structure capable of generating such a rich collection of charged and neutral walls. However, the hexagonal tungsten bronze system, $CsNbW_2O_9$, has recently been shown to have strikingly similar characteristics to the manganites, including an apparently almost identical meandering ferroelectric domain microstructure. Such uncanny similarities suggest the strong possibility of conducting domain walls, thereby making $CsNbW_2O_9$ another potential candidate for domain wall nanoelectronics.[17] In our previous work, powder neutron diffraction and powder x-ray diffraction were used to reveal the structural evolution of $CsNbW_2O_9$ with temperature.[17] The improper ferroelectricity arises from the coupling of the K_3 mode and the Γ_2^- mode during the ferroelectric transition at 1100 K ($P6/mmm \rightarrow P6mm$), and unit cell tripling occurs in the form of "two-up, one-down" cation displacements (associated with the K_3 mode). Although the symmetry modes involved are reminiscent of the manganites,[18] here, displacements occur on both the A sites and the B sites (more prominently on the B sites) and are driven by second order Jahn–Teller distortions in contrast to the tilt- (geometry-) driven ferroelectric transition in the manganites. $CsNbW_2O_9$ also undergoes a tilt transition, but at lower temperature—below 350 K—where tilting of the BO_6 polyhedra, described by an A_3^+ mode, results in similar "all-in, all-out" octahedral trimerization (mimicking the manganites once again), giving the same space group of the manganite ferroelectric phase ($P6_3cm$). However, it is important to stress that in $CsNbW_2O_9$, the tilting does not result in the formation of the domain microstructure, which forms at $T_C \sim 1100$ K. [Note that $CsNbW_2O_9$ undergoes a final phase transition at 300 K causing a small orthorhombic distortion and octahedral tilting in the basal plane arising from the A_6^+ mode ($P6_3cm \rightarrow Cmc2_1$), but again, this has no implication for the ferroelectric domain microstructure described herein].

Transmission electron microscopy (TEM) and piezoresponse force microscopy (PFM) studies revealed a similar domain structure to that of the manganites,[17] reinforcing the apparent analogous nature of the two systems. Commonality in microstructure was attributed to the similarities in symmetry breaking and resultant dipole configurations: three translational variants denoted as α, β, and γ (in keeping with the convention used for the manganites) arising from the cell tripling, combined with two polar variants (+ and −), allow the characteristic sixfold cloverleaf domain configuration to also form in the hexagonal tungsten bronzes. Figure 1 compares the domain structure of $ErMnO_3$ to that observed in $CsNbW_2O_9$. It is clear that the meandering domain walls and cloverleaf vertices are common to both. Noting the scale bars, it is evident that the domain/vertex density of $CsNbW_2O_9$ is much greater than that observed in the $ErMnO_3$ sample shown in Fig. 1(c). However, it has been shown that the domain density of the manganites is dependent on the cooling rate during sample preparation, and thus, identical domain structures on a similar, sub-micron length scale to that of $CsNbW_2O_9$ are also entirely possible in the manganites.[19]

In the manganites, the domains walls can adopt any orientation with respect to the polar axis, resulting in domain wall sections that are charged and sections, which are neutral (with the latter reminiscent of 180° domain walls observed in proper ferroelectrics). The sections that are charged are responsible for a divergence of polarization and may exhibit enhanced or diminished conduction, while neutral sections typically show no enhanced or diminished conduction relative to the bulk.[10] It should be noted that any inclination of the wall beyond a parallel alignment to the polar axis results in a non-zero divergence of polarization, meaning that the section of the wall will be somewhat charged and show enhanced/diminished conduction. However, this varies with inclination angle as the normal polarization component to the wall will vary sinusoidally with inclination also. Consequently, the conduction properties of the charged wall sections have been shown to vary with respect to their alignment to the polarization direction.[10]

In our previous work on $CsNbW_2O_9$, it was noted that no enhanced/diminished domain wall conduction had yet been observed with conductive atomic force microscopy (c-AFM) measurements. It was postulated that a percolative current pathway from the base electrode to the AFM tip had not been established due to the granular nature of the ceramic sample. An alternative explanation for the lack of observed domain wall conduction is provided herein based on more recent findings. Using both TEM and PFM, a comprehensive description of the ferroelectric domain structure in three spatial dimensions is herein reported, qualifying the previously reported description of its nature based on 2D projections. It is proposed that although the domain structure of $CsNbW_2O_9$ appears strikingly similar to that of the manganites, its meandering nature is mainly restricted to two dimensions (the *ab* plane) as opposed to three dimensions (as in the manganites) as a result of the differences in crystal structure. $CsNbW_2O_9$ consists of hexagonal configurations of interconnected BO_6 (B = W, Nb) polyhedra forming the Cs-containing channels, while the manganite structure consists of alternating layers of MnO_5 polyhedra and *R* cations. The 3D connectivity between BO_6 polyhedra in $CsNbW_2O_9$ means that the domain walls are constrained to run parallel to the polar axis. Thus, the charged head-to-head or tail-to-tail domain wall configurations, which lead to enhanced/diminished domain wall conduction arising from local band bending and accumulation of charge carriers, are not favored in this material.

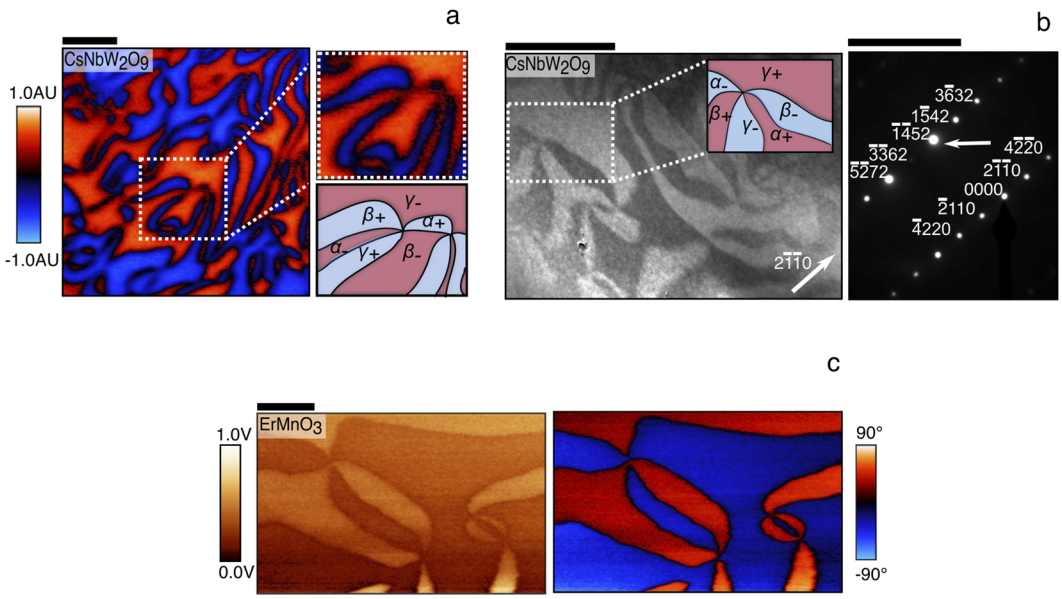

FIG. 1. (a) Lateral PFM $R\cos\theta$ map of the domain structure of $CsNbW_2O_9$, where the amplitude at each point is multiplied by the cosine of the phase (helpful for clarity due to limited resolution of vertices at this small length scale). Scale bar represents 500 nm. (b) $CsNbW_2O_9$ dark field TEM image of the cloverleaf domain configuration along a direction close to the ***c***-axis, obtained using the $\bar{1}\bar{4}52$ diffraction spot as indicated by the arrow in the accompanying diffraction pattern of the $[0\bar{2}\bar{2}9]$ zone axis, to which the sample was aligned. The scale bars for the dark field image and diffraction pattern represent 500 nm and 5 nm^{-1}, respectively. (c) Lateral PFM amplitude (left) and phase (right) maps of $ErMnO_3$, showing the sixfold cloverleaf domain structure similar to that observed in (a) and (b). Scale bar represents 4 μm.

II. EXPERIMENTAL METHOD

The domain microstructure of various grains was imaged using PFM. In order to study the domain microstructure of $CsNbW_2O_9$ with respect to its crystal structure, vector PFM was performed on a grain of interest. Generally, PFM is an imaging technique that cannot exactly determine the crystallographic direction being imaged and is therefore unhelpful in constructing a 3D description of the domain structure. However, as this system is expected to display uniaxial polarization, the direction of the lateral polarization component can be estimated by rotating a sample with a grain having the polarization approximately in the surface plane and examining the amplitude of the piezoresponse as a function of sample orientation. PFM measurements were performed using an Asylum Research MFP-3D atomic force microscope.

The domain structure was then observed using TEM from different projection directions, using several different lamellae prepared from different grains in a ceramic of $CsNbW_2O_9$, so that a statistical reconstruction of the form of the domain structure in three dimensions could be made. All TEM work was performed with a FEI Tecnai T20 operated at 200 kV in both tilted dark field and selected area diffraction (SAD) modes, with all data being recorded using an Olympus SIS Megaview III CCD camera and a Gatan Imaging Filter (GIF) CCD camera. The dark field imaging mode was used to image the domain structure in the TEM using the smallest possible objective aperture to select just the diffraction spot of interest to form the image. This provides the only approach to obtain domain contrast for this system due to its uniaxial polarization. As the material only supports 180° domains, there is no diffraction contrast from crystal tilts due to ferroelastic distortions and lattice matching at grain boundaries.[20] Contrast can arise using the dark field mode due to the breakdown of Friedel's law for a non-centrosymmetric crystal undergoing dynamical diffraction.[21,22] Thus, the intensity of two opposing reflections (related by inversion symmetry), when aligned exactly on a zone axis, will not be equal if they have at least a component along the polarization direction, i.e., if $\mathbf{g}\cdot\mathbf{P}\neq 0$,

$$I(\mathbf{g}) \neq I(-\mathbf{g}). \quad (1)$$

Using a suitable reflection in dark field mode, domains with opposing polarization in a uniaxial system (180° domains) should give intensity contrast due to the failure of Friedel's law. It is this mechanism that is exploited in an attempt to reconstruct the domain structure in three dimensions. Following the work in our previous publication,[17] the hexagonal system of indexing ($P6_3cm$) will be used rather than the orthorhombic system, as the negligible orthorhombic distortion precludes the ability to distinguish unique directions in the orthorhombic cell unambiguously using conventional selected area diffraction (SAD) methods for all except very few crystal directions (see the supplementary material for the matrix transformations for interchanging between the two indexing systems).

III. RESULTS AND DISCUSSION

Figure 2 shows vector PFM of a grain with a highly linear domain configuration. Such grains were observed far less frequently than those that exhibit the cloverleaf structure. Although highly linear, it is clear there is a slight cloverleaf component (the walls meander slightly), similar to that seen in Fig. 1. The observed

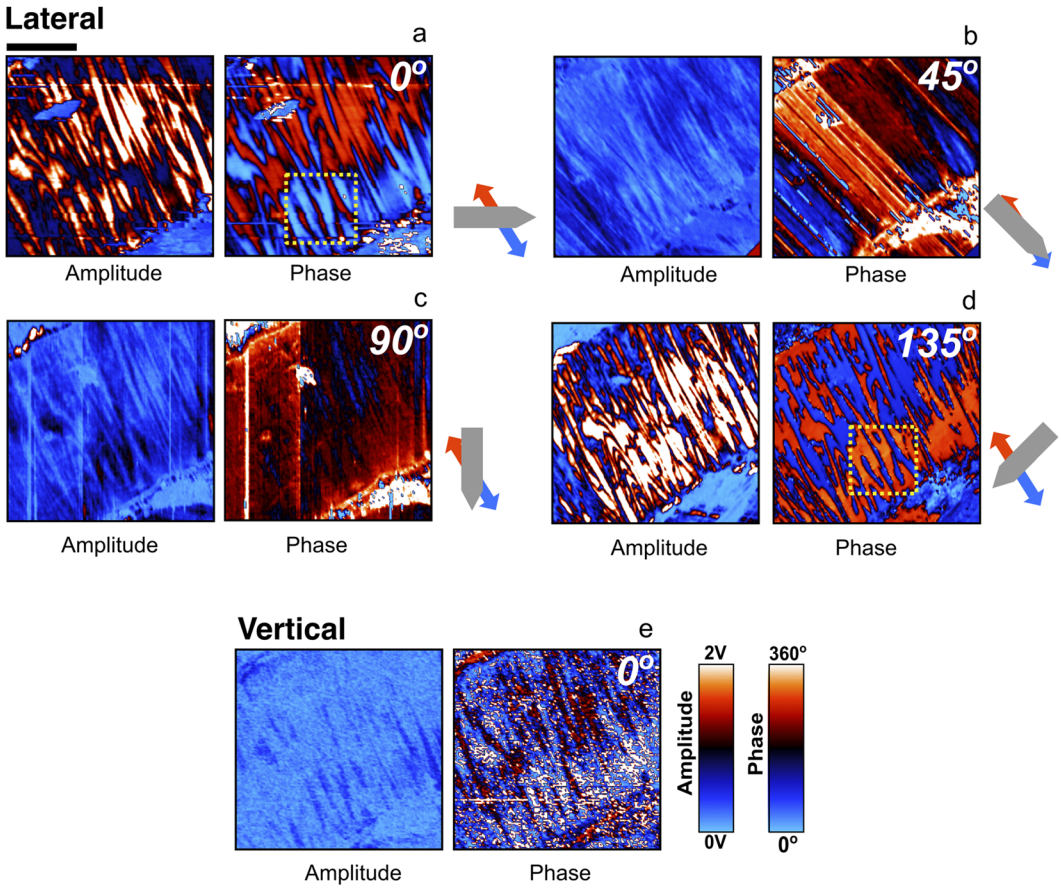

FIG. 2. Vector-resolved PFM data. (a) Lateral PFM of a grain exhibiting a highly linear type domain structure. The same region is imaged at a variety of angles with respect to the initial scan—(b) 45°, (c) 90°, and (d) 135° as indicated by the schematic of the cantilever alongside. The approximate inferred polar axes are also shown by red and blue arrows. (e) shows vertical PFM of the same region (taken at the angle of the initial scan angle of 0°) demonstrating a predominantly in-plane polarization. The yellow dotted box in (a) and (d) illustrates the phase inversion due to the cantilever rotation. Scale bar represents 3 μm.

hybrid microstructure in Fig. 2 suggests that the apparent distinction between the linear and cloverleaf microstructures may, in fact, be as a result of the crystallographic direction being viewed, rather than the presence of the two distinct domain configurations. The anisotropy of the microstructure, i.e., the direction of the stripes, is evaluated with respect to the orientation at which maximum lateral piezoresponse is obtained. This is used to estimate the polarization direction relative to the stripes given that this grain shows a very weak out-of-plane signal [Fig. 2(e)], and perpendicular alignment of the cantilever with the polar axis generates the greatest lateral response. However, it should be noted that some weak stripe contrast in Fig. 2(e) indicates a small out-of-plane component. The vector PFM suggests the possibility that the domains/domain walls in this grain may run along or close to the polar axis. This is demonstrated by the data shown in Fig. 2. The topography (not shown) ensures that the region being probed is mostly flat with little topographic variations. Lateral PFM (LPFM) images acquired at various sample orientations are displayed in Figs. 2(a)–2(d), where the relative orientation of the cantilever body and hypothesized polar axis are indicated for each scan by the cartoons alongside. The angle beside each image describes the orientation of the sample, referenced to the initial scan undertaken at 0°. It is clear that a strong signal is measured both in the amplitude and phase channels at 0°. Upon rotation by 45°, the signal in both channels almost entirely disappears and is only very weakly visible at 90°. The original signal is fully retrieved upon rotation by 135°, appearing marginally stronger than at 0°, suggesting that the lateral alignment of the polarization lies between these directions, but closer to 135°. It is expected that the strongest LPFM signal should occur when the cantilever body and the polar axis are perpendicularly aligned, as the amplitude and direction of axial cantilever twisting determines the LPFM amplitude and phase, respectively. This also explains the phase inversion (illustrated by the yellow dotted boxes) observed between the angles of 0° and 135°, where red domains become blue (and vice versa). Between these scans, the direction of the force associated with the polarization will reverse in the cantilever frame of reference, thus yielding opposing LPFM phases for the two cases. Summing up the vector PFM data displayed in Figs. 2(a)–2(d), it appears probable

that the linear, stripe-like domains share the same axis as the polarization. It seems likely that the observed stripe-like domains are the result of viewing the domain structure perpendicular to the polar axis and that the cloverleaf structure, illustrated in Fig. 1, is observed when viewed from a direction parallel to the polarization. The slight cloverleaf components may be explained by the small out-of-plane component [Fig. 2(e)] as a result of the polished surface cutting through the crystal structure at some angle slightly less than 90° to the polar axis.

The hypothesis that the stripe domains (and hence domain walls) run along or close to the *c*-direction was confirmed using TEM by imaging the domain structure from different viewing directions. The range of projection directions is achieved by slicing lamellae at different crystallographic orientations from the bulk ceramic. The range of projection directions that are used to generate the 3D reconstruction are defined as those with varied angles with the [0001] pole in any vertical plane—(hki0). This is shown schematically in Fig. 3. The azimuthal angle, ϕ, is not considered of great importance given the high degree of symmetry in the basal plane (following the assumption that the system should be considered pseudohexagonal). The planar cut of the lamella is therefore defined by the elevation angle, θ, from the [0001] direction—the unique polar axis.

For samples where it was not possible to reach the [0001] pole within the tilt range of the microscope stage, θ is estimated by aligning the grain on the nearest zone axis to the neutral stage position in the microscope, determining the beam direction for this zone axis and then calculating the angle between that zone axis and [0001] based on a standard crystallographic calculation (see Figs. S2–S4 of the supplementary material). Otherwise, θ is determined from the α and β tilt values required to reach the [0001] pole. In addition, the determination of θ in each case makes several further assumptions and therefore has a relatively large associated uncertainty. It assumes parallel alignment of the lamella on the Omniprobe finger (void of any bend contours) and that the Omniprobe grid sits untilted (horizontal) in the microscope for the neutral stage position. Therefore, the values quoted for θ are given with the relatively large uncertainty of ±10°. The corresponding diffraction patterns show the reflection used to obtain the image, in keeping with the conditions aforementioned. Figure 4 shows the domain structure and corresponding diffraction patterns from various lamellae for θ values of 30°, 50°, 80°, and 90°. The image of the domain structure in Fig. 1(b) was obtained for the same sample shown in Fig. 4(a) (a θ value of ~30°).

It is clear that at higher values of θ such that the lamella almost contains the polar axis (80° and 90°), a more linear, stripe-like domain configuration is observed. For the lower values of 30° and 50° [Figs. 4(a) and 4(c)], the characteristic cloverleaf domain structure is observed, although a notable elongation of domain walls along the *c*-axis appears at 50°. Thus, as θ increases, the observed domain configuration becomes more linear. The observation of

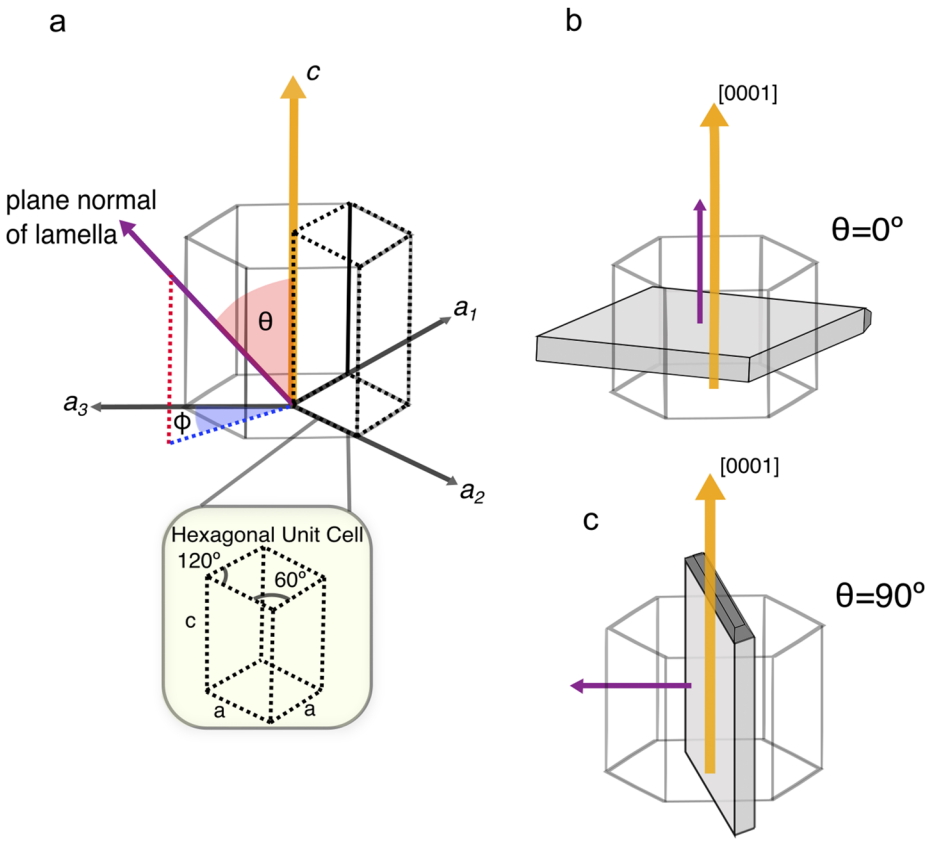

FIG. 3. (a) Schematic diagram showing how the lamella plane cut is defined with reference to the hexagonal unit cell. (b) and (c) show the orientation of a lamella cut with $\theta = 0°$ and $\theta = 90°$, respectively, with respect to the [0001] direction.

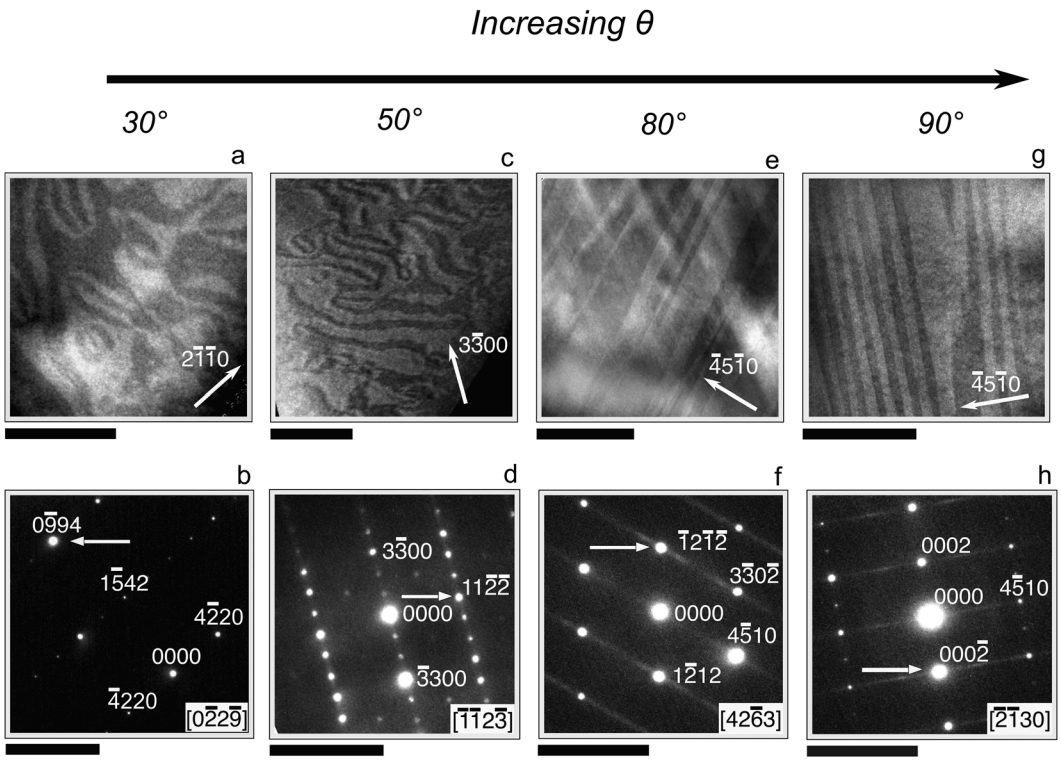

FIG. 4. (a) Dark field image of the domain structure of $CsNbW_2O_9$ from a lamella orientated at θ = 30°, obtained using the $0\bar{9}94$ reflection as indicated by the arrow in the corresponding [$0\bar{2}2\bar{9}$] diffraction pattern shown in (b). (c) Dark field image obtained at θ = 50° with the corresponding diffraction pattern shown in (d). (e) and (f) show the dark field image and corresponding diffraction pattern, respectively, for θ = 80°. (g) and (h) show the dark field image and corresponding diffraction pattern, respectively, for θ = 90°. In each case, the reflection used to obtain the image is indicated by the white arrow in the diffraction pattern with the zone axis indicated in the bottom right-hand side corner. Scale bars on dark field images (a), (c), (e), and (g) represent 500 nm, and the scale bar on diffraction patterns (b), (d), (f), and (h) represent 5 nm^{-1}.

increasing linearity with θ in the TEM data indicates high anisotropy inherent in the domain configuration in which the domain walls are confined to run along or close to the *c*-axis and only meander in the basal plane, i.e., neutral domain walls are favored over charged sections. This is an important distinction from the manganite domain structure, which often meanders isotropically in all three dimensions.[23] The presence of a linear domain structure can also be observed in the SAD data in which diffuse streaking is observed along directions perpendicular to the *c*-axis [Figs. 4(f) and 4(h)]. The effect observed is that of the domain walls disturbing the periodicity of the diffracting planes for incoming electrons. The diffuse streaking along directions perpendicular to [0001] confirms that the domain walls run parallel to [0001] and do not have a definite periodicity; otherwise coherent spots would appear in these directions (although with a very short period).

The TEM data strongly corroborates the vector-PFM data and the claim that the domain walls lie predominantly on planes that contain the *c*-axis, i.e., neutral domain wall sections are favored. While the manganite structure permits domain walls the freedom to meander in all three dimensions, the walls in $CsNbW_2O_9$ are confined to meander in two—the *ab* plane. A schematic of the proposed domain microstructure is presented in Fig. 5. As θ increases, the observed domain structure transforms from the cloverleaf structure, reminiscent of the manganites, to a much more linear configuration as θ approaches 90°. The observed transformation is obviously gradual and therefore only becomes highly linear at angles close to 90°. Caution should therefore be taken when interpreting PFM data of such a microstructure, as the LPFM images shown in Fig. 1 appear to show the presence of charged domain walls; however, the inclination of these walls with respect to the polished surface means that they are in fact uncharged. This new insight unveils a completely unique domain microstructure that possesses characteristics of the rare earth manganites, in the form of the meandering domain walls and cloverleaf motifs, but also exhibits inherent anisotropy, confining the dimensions in which the domain walls can meander.

The anisotropy has some important implications for the potential application of this material. The fact that domain walls do not appear to meander away from planes containing the *c*-axis means that potential functionality associated with charged domain walls is inhibited, specifically domain wall electrical conductivity. It is well known that domain wall conduction in the manganites arises due to the polarization discontinuity at domain walls in which the wall normal is not completely orthogonal to the polar axis.[10] The alike bound charges generated either side of a "head-to-head" or "tail-to-tail" domain wall require mobile charge carriers to screen the

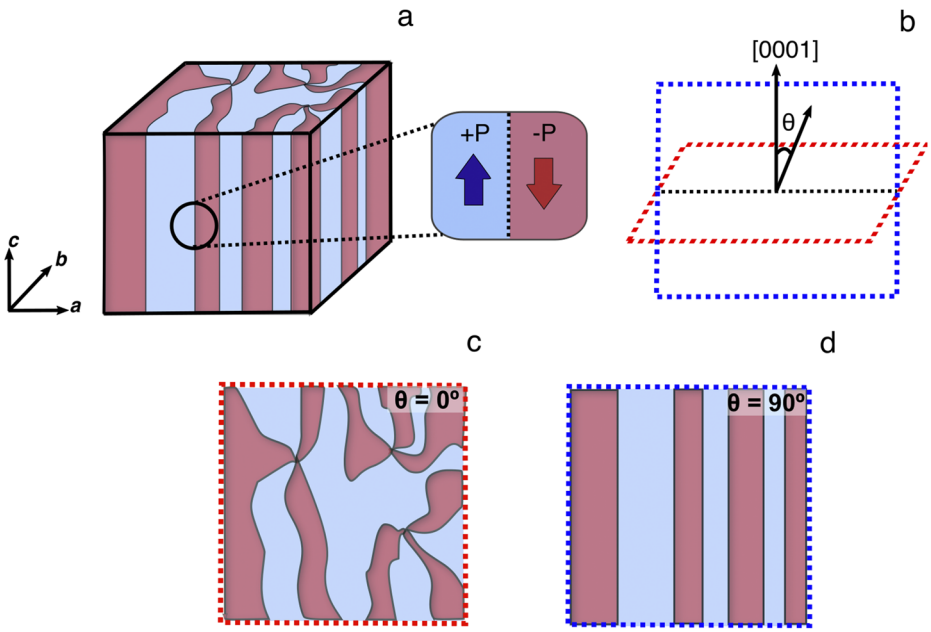

FIG. 5. (a) Schematic of the domain configuration in three spatial dimensions (colored arrows denote polarization vector). (b) Projection planes parallel and perpendicular to the polar axis. [(c) and (d)] Domain structure observed from projection directions denoted in (b).

unfavorable divergent electric displacement,[10] and electrostatic band bending is induced in the vicinity of the wall, corresponding to a reduction in the conduction band energy toward the Fermi energy at head-to-head walls or an increase in the valence band energy toward the Fermi energy at tail-to-tail walls.[24,25] The combination of these mechanisms results in enhanced conduction at "tail-to-tail" walls facilitated by mobile holes[10] and eventual activation of enhanced conduction at "head-to-head" walls above sufficient bias.[25] The latter of these driving mechanisms is obviously aided by a smaller bandgap, so already, $CsNbW_2O_9$ is at a disadvantage given the comparably larger bandgap (2.38 eV)[26] to that of the manganites (1.3 eV–1.6 eV).[27] Furthermore, the relationship between domain wall conduction and inclination angle to the polar axis in the manganites demonstrates that neutral walls should not show any enhanced conduction relative to the bulk.[10] It should be noted however that nominally neutral walls have been shown to exhibit enhanced DC or AC conduction in some cases; however, this is typically associated with extrinsic defect mediated conduction such as the accumulation of oxygen interstitials[28,29] or the domain wall oscillation mode when the polarization is aligned with an applied AC field.[30] Intrinsic contributions to domain wall conduction, however, are solely associated with band bending at "head-to-head" or "tail-to-tail" charged wall configurations.[10,28] Such configurations can obviously not be realized in $CsNbW_2O_9$ if the walls do not meander away from planes containing the *c*-axis. This provides insight into why significant domain wall conduction was not observed in this material using conductive-AFM.

Given the strikingly similar characteristics in symmetry breaking and dipole configuration, such a discovery is quite surprising. Therefore, in order to understand the slightly differing domain microstructure, it is important to consider the domain wall structure in light of some of the differences in the crystal structures of the manganites compared to $CsNbW_2O_9$. Both undergo similar transitions in terms of symmetry-breaking modes on entering the polar phase; the same unit cell tripling in the *ab* plane as a result of the K_3 mode gives rise to translational antiphase boundaries (APBs), which interlock with the ferroelectric boundaries to give the characteristic sixfold cloverleaf domain vertices. In the manganites, two types of domain wall have been observed, associated with the two possible APBs with either *a*/3 or 2*a*/3 displacement, and appear to have differing frequency of occurrence depending on the section of the sample viewed.[31] Although the precise structure and frequency of occurrence of these have yet to be observed experimentally in $CsNbW_2O_9$, simple consideration of the symmetry and structure requires these for the generation of the sixfold vertices[17] (see also Fig. S5 of the supplementary material). Although the sixfold domain vertices in the *ab* plane are the same in both materials, the anisotropic nature of domain formation in $CsNbW_2O_9$, specifically the apparent absence of domain wall sections that are charged and which give rise to bound charges associated with a divergence in *P*, may simply be rationalized in the context of two key structural differences compared to the manganites:

(1) In $CsNbW_2O_9$, the origin of the K_3 mode is purely displacive due to B-cation off-centering via the second order Jahn–Teller effect—this is an electronic mechanism in contrast to the geometrically driven K_3 mode in the manganites where the MnO_5 polyhedral tilting ("trimerization") results in displacements of the A cations [Fig. 6(a)].
(2) The hexagonal manganites have a layered structure with sheets of MnO_5 polyhedra in the *ab*-plane separating the A-layers, which generate the polarization, whereas in the HTB structure of $CsNbW_2O_9$, the displaced BO_6 octahedra that give rise to the polarization are connected in all three dimensions (therefore importantly along the polar *c*-axis).

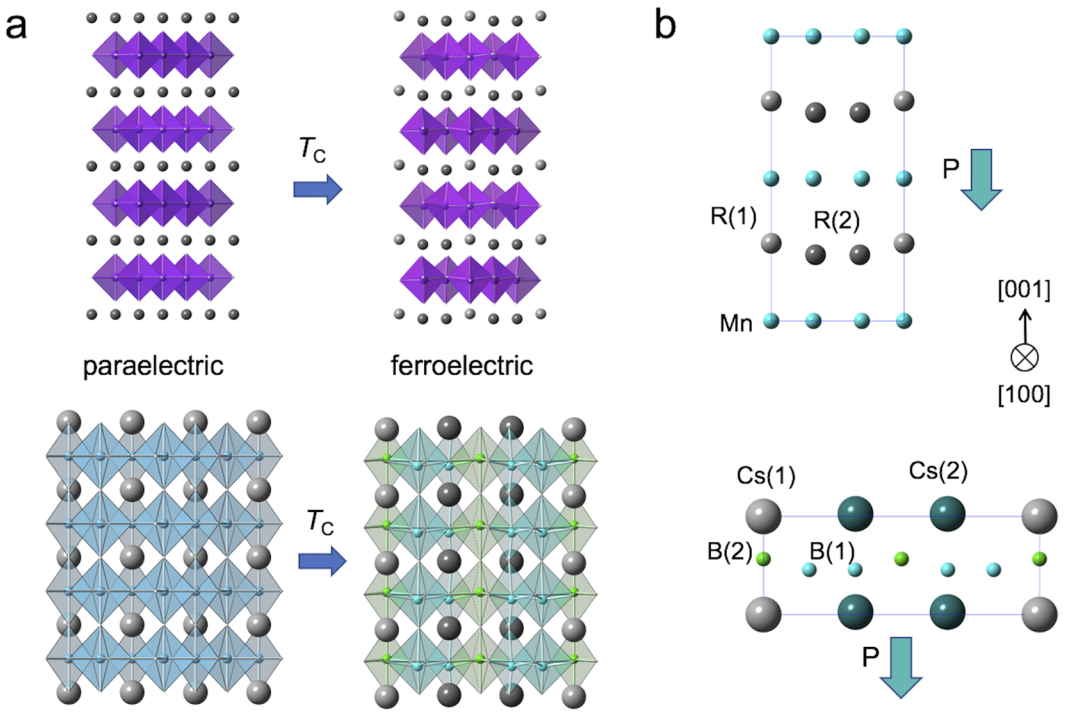

FIG. 6. Crystal models of the paraelectric and ferroelectric phases of $R\mathrm{MnO_3}$ (top) and $\mathrm{CsNbW_2O_9}$ (bottom), respectively (a). It can be seen that the distortion to the $R\mathrm{MnO_3}$ structure involves significant octahedral tilting or "trimerization," whereas the distortion to the $\mathrm{CsNbW_2O_9}$ structure is dominated by the purely vertical displacement of the Nb/W cations (tilting occurs at lower temperature transition). (b) Resulting unit cells for the ferroelectric phases indicating the two-up one-down cation displacements in both $R\mathrm{MnO_3}$ (top) and $\mathrm{CsNbW_2O_9}$ (bottom). Note that for clarity, oxygen atoms have been omitted in all cases.

As mentioned previously, it should be noted that octahedral tilting (reminiscent of the trimerization mechanism of manganites) does occur in HTB, but at a lower phase transition temperature of 350 K, after the domain structure has been established and locked in at T_C = 1100 K, so in contrast to the manganites, the "trimerization" has little or no effect on the already established domain structure in HTB. In the manganites, the tilting induces the atomic displacements, and so, both happen within the one transition, whereas in $\mathrm{CsNbW_2O_9}$, these are spread over separate phase transitions.

For both systems, the resulting "two-up, one-down" cation displacements give rise to the polarization in *c* [Fig. 6(b)]. In the manganites, the $\mathrm{MnO_5}$ tilting gives rise to very little or no displacement of the Mn cations in the *c*-axis,[32] and the A cation displacements have the largest contribution to the total polarization of ~4 μC cm^{-2} to 6 μC cm^{-2}; in contrast, the B-cation displacements in $\mathrm{CsNbW_2O_9}$ dominate and give a higher net polarization of ~13 μC cm^{-2} (see Fig. S9 of the supplementary material). In the manganites, the formation of the charged (head-to-head or tail-to-tail) wall sections has also been shown to result from interlocking of antiphase and ferroelectric domain boundaries. The incorporation of this translation shift of either *a*/3 or 2*a*/3 of the unit cell in either side of the charged wall reduces the energy cost of the wall significantly by reducing the number of opposing A-cation displacements on either side of the wall.[31,33,34] Density functional theory (DFT) calculations[24] for $R\mathrm{MnO_3}$ have shown that inclusion of an APB (60° phase shift) to form either $\alpha^-|\beta^+$, $\alpha^-|\gamma^+$, or $\beta^-|\gamma^+$ charged domain wall section has conformation energies of ~110 mJ m^{-2} compared to ~250 mJ m^{-2} for a simple ferroelectric $\alpha^-|\alpha^+$ (180° phase shift) charged wall—an energy saving of ~140 mJ m^{-2}. In addition to the energy lowering afforded by this phase shift, it appears that the relatively unperturbed $\mathrm{MnO_5}$ polyhedral layers essentially act as "buffers" to minimize the electrostatic interactions between the oppositely displaced A-cations on either side of the charged domain wall.

Although a similar charged wall structure is possible in $\mathrm{CsNbW_2O_9}$ whereby incorporation of a translational boundary (APB) reduces by two thirds the number of opposing displacements (see Figs. S6–S8 of the supplementary material), the connectivity of the $\mathrm{BO_6}$ octahedra along the polar *c*-axis does not afford the same buffering effect. Due to the high positive charge, and hence polarization, associated with the displaced $\mathrm{W^{6+}}$ and $\mathrm{Nb^{5+}}$ cations, the necessary head-to-head or tail-to-tail configuration for connected polyhedra either side of a charged domain wall structure appears to be energetically too costly in $\mathrm{CsNbW_2O_9}$. In addition, the small correlated displacements of $\mathrm{Cs^+}$ ions in the hexagonal channels running along the *c*-axis will contribute to the electrostatic energy cost of such charged wall sections given that the $\mathrm{Cs^+}$ ions are essential unscreened from each other in this axis.

IV. CONCLUSION AND SUMMARY

In summary, the domain structure of $CsNbW_2O_9$ has been studied from a range of projection directions using TEM in order to reconstruct the configuration in three spatial dimensions. It has been shown that the domain structure exhibits high anisotropy such that, although the domain walls meander in the *ab* plane, they are confined to run along the *c* axis. The findings are corroborated by vector-PFM measurements. This is attributed to the confinement of atomic displacements to the ±[0001] direction during the paraelectric–ferroelectric transition and the connectivity of atomic layers along this direction. As a result, the desirable head-to-head or tail-to-tail (charged) domain wall configurations largely associated with enhanced or diminished domain wall conduction have not been realized in this material to date.

SUPPLEMENTARY MATERIAL

See the supplementary material for the crystallographic indexing system used in this work, the calculation of the tilts of each specimen normal away from the *c*-axis, and the charge on different types of walls possible in $CsNbW_2O_9$ and on the contributors to the polarization in this material and $YMnO_3$ that it is compared to.

ACKNOWLEDGMENTS

S.J.M. acknowledges the EPSRC-funded CDT in Photonic Integration and Advanced Data Storage (Grant No. EP/L015323/1) for his Ph.D. studentship under which the work at the University of Glasgow was carried out. The work at Queen's University Belfast and the University of St Andrews was carried out as part of an EPSRC-funded collaboration (Grant Nos. EP/P02453X/1 and EP/P024637/1).

DATA AVAILABILITY

The data that support the findings of this study are openly available in Enlighten: Research Data at https://doi.org/10.5525/gla.researchdata.1052.

REFERENCES

[1] A. Aird and E. K. H. Salje, J. Phys.: Condens. Matter **10**, L377 (1998).
[2] S. Farokhipoor, C. Magén, S. Venkatesan, J. Íñiguez, C. J. M. Daumont, D. Rubi, E. Snoeck, M. Mostovoy, C. De Graaf, A. Müller, M. Döblinger, C. Scheu, and B. Noheda, Nature **515**, 379 (2014).
[3] S. Van Aert, S. Turner, R. Delville, D. Schryvers, G. Van Tendeloo, and E. K. H. Salje, Adv. Mater. **24**, 523 (2012).
[4] J. P. V. McConville, H. Lu, B. Wang, Y. Tan, C. Cochard, M. Conroy, K. Moore, A. Harvey, U. Bangert, L. Q. Chen, A. Gruverman, and J. M. Gregg, Adv. Funct. Mater. **30**, 2000109 (2020).
[5] J. Seidel, L. W. Martin, Q. He, Q. Zhan, Y.-H. Chu, A. Rother, M. E. Hawkridge, P. Maksymovych, P. Yu, M. Gajek, N. Balke, S. V. Kalinin, S. Gemming, F. Wang, G. Catalan, J. F. Scott, N. A. Spaldin, J. Orenstein, and R. Ramesh, Nat. Mater. **8**, 229 (2009).
[6] M. Schröder, A. Haußmann, A. Thiessen, E. Soergel, T. Woike, and L. M. Eng, Adv. Funct. Mater. **22**, 3936 (2012).
[7] T. Sluka, A. K. Tagantsev, P. Bednyakov, and N. Setter, Nat. Commun. **4**, 1808 (2013).
[8] Y. S. Oh, X. Luo, F.-T. Huang, Y. Wang, and S.-W. Cheong, Nat. Mater. **14**, 407 (2015).
[9] R. G. P. McQuaid, M. P. Campbell, R. W. Whatmore, A. Kumar, and J. M. Gregg, Nat. Commun. **8**, 15105 (2017).
[10] D. Meier, J. Seidel, A. Cano, K. Delaney, Y. Kumagai, M. Mostovoy, N. A. Spaldin, R. Ramesh, and M. Fiebig, Nat. Mater. **11**, 284 (2012).
[11] G. Catalan, J. Seidel, R. Ramesh, and J. F. Scott, Rev. Mod. Phys. **84**, 119 (2012).
[12] J. R. Whyte and J. M. Gregg, Nat. Commun. **6**, 7361 (2015).
[13] G. Sanchez-Santolino, J. Tornos, D. Hernandez-Martin, J. I. Beltran, C. Munuera, M. Cabero, A. Perez-Muñoz, J. Ricote, F. Mompean, M. Garcia-Hernandez, Z. Sefrioui, C. Leon, S. J. Pennycook, M. C. Muñoz, M. Varela, and J. Santamaria, Nat. Nanotechnol. **12**, 655 (2017).
[14] M. P. Campbell, J. P. V. McConville, R. G. P. McQuaid, D. Prabhakaran, A. Kumar, and J. M. Gregg, Nat. Commun. **7**, 13764 (2016).
[15] P. W. Turner, J. P. V. McConville, S. J. McCartan, M. H. Campbell, J. Schaab, R. G. P. McQuaid, A. Kumar, and J. M. Gregg, Nano Lett. **18**, 6381 (2018).
[16] C. J. Fennie and K. M. Rabe, Phys. Rev. B **72**, 100103 (2005).
[17] J. A. McNulty, T. T. Tran, P. S. Halasyamani, S. J. McCartan, I. MacLaren, A. S. Gibbs, F. J. Y. Lim, P. W. Turner, J. M. Gregg, P. Lightfoot, and F. D. Morrison, Adv. Mater. **31**, 1903620 (2019).
[18] B. B. Van Aken, T. T. M. Palstra, A. Filippetti, and N. A. Spaldin, Nat. Mater. **3**, 164 (2004).
[19] S. M. Griffin, M. Lilienblum, K. T. Delaney, Y. Kumagai, M. Fiebig, and N. A. Spaldin, Phys. Rev. X **2**, 041022 (2012).
[20] M. U. Farooq, R. Villaurrutia, I. MacLaren, H. Kungl, M. J. Hoffmann, J.-J. Fundenberger, and E. Bouzy, J. Microsc. **230**, 445 (2008).
[21] F. Fujimoto, J. Phys. Soc. Jpn. **14**, 1558 (1959).
[22] M. Tanaka and G. Honjo, J. Phys. Soc. Jpn. **19**, 954 (1964).
[23] T. Jungk, Á. Hoffmann, M. Fiebig, and E. Soergel, Appl. Phys. Lett. **97**, 012904 (2010).
[24] D. R. Småbråten, Q. N. Meier, S. H. Skjærvø, K. Inzani, D. Meier, and S. M. Selbach, Phys. Rev. Mater. **2**, 114405 (2018).
[25] J. A. Mundy, J. Schaab, Y. Kumagai, A. Cano, M. Stengel, I. P. Krug, D. M. Gottlob, H. Doğanay, M. E. Holtz, R. Held, Z. Yan, E. Bourret, C. M. Schneider, D. G. Schlom, D. A. Muller, R. Ramesh, N. A. Spaldin, and D. Meier, Nat. Mater. **16**, 622 (2017).
[26] L. Li, H. Xu, Y. Chen, and Y. Wang, Opt. Mater. **66**, 361 (2017).
[27] X. Huang, T. R. Paudel, S. Dong, and E. Y. Tsymbal, Phys. Rev. B **92**, 125201 (2015).
[28] J. Schultheiß, J. Schaab, D. R. Småbråten, S. H. Skjærvø, E. Bourret, Z. Yan, S. M. Selbach, and D. Meier, Appl. Phys. Lett. **116**, 262903 (2020).
[29] J. Schaab, S. H. Skjærvø, S. Krohns, X. Dai, M. E. Holtz, A. Cano, M. Lilienblum, Z. Yan, E. Bourret, D. A. Muller, M. Fiebig, S. M. Selbach, and D. Meier, Nat. Nanotechnol. **13**, 1028 (2018).
[30] X. Wu, U. Petralanda, L. Zheng, Y. Ren, R. Hu, S. W. Cheong, S. Artyukhin, and K. Lai, Sci. Adv. **3**, e1602371 (2017).
[31] Q. H. Zhang, L. J. Wang, X. K. Wei, R. C. Yu, L. Gu, A. Hirata, M. W. Chen, C. Q. Jin, Y. Yao, Y. G. Wang, and X. F. Duan, Phys. Rev. B **85**, 020102 (2012).
[32] A. S. Gibbs, K. S. Knight, and P. Lightfoot, Phys. Rev. B **83**, 094111 (2011).
[33] T. Matsumoto, R. Ishikawa, T. Tohei, H. Kimura, Q. Yao, H. Zhao, X. Wang, D. Chen, Z. Cheng, N. Shibata, and Y. Ikuhara, Nano Lett. **13**, 4594 (2013).
[34] M.-G. Han, Y. Zhu, L. Wu, T. Aoki, V. Volkov, X. Wang, S. C. Chae, Y. S. Oh, and S.-W. Cheong, Adv. Mater. **25**, 2415 (2013).